De novo disease-associated mutations in KIF1A dominant negatively inhibit axonal transport of synaptic vesicle precursors

Yuzu Anazawa[1,4], Tomoki Kita[2,4], Kumiko Hayashi[2] and Shinsuke Niwa[1,3,#]

[1]Graduate school of Life Sciences, Tohoku University, Katahira 2-1, Aoba-ku, Sendai, Miyagi 980-8578, Japan

[2]Department of Applied Physics, Graduate school of Engineering, Tohoku University, Aramaki-Aoba 6-6-05, Aoba-ku, Sendai, Miyagi, Japan

[3]Frontier Research Institute for Interdisciplinary Sciences (FRIS), Tohoku University, Aramaki-Aoba 6-3, Aoba-ku, Sendai, Miyagi 980-0845, Japan

[4]These authors contributed equally to this work

[#]Corresponding author:

SHINSUKE NIWA, Frontier Research Institute for Interdisciplinary Sciences (FRIS), Tohoku University, Aramaki-Aoba 6-3, Aoba-ku, Sendai, Miyagi 980-0845, Japan

e-mail: shinsuke.niwa.c8@tohoku.ac.jp

Abstract

KIF1A is a kinesin superfamily molecular motor that transports synaptic vesicle precursors in axons. Mutations in *Kif1a* lead to a group of neuronal diseases called KIF1A-associated neuronal disorder (KAND). KIF1A forms a homodimer and KAND mutations are mostly *de novo* and autosomal dominant; however, it is not known whether the function of wild-type KIF1A is inhibited by disease-associated KIF1A. No reliable *in vivo* model systems to analyze the molecular and cellular biology of KAND have been developed; therefore, here, we established *Caenorhabditis elegans* models for KAND using CRISPR/cas9 technology and analyzed defects in axonal transport. In the *C. elegans* models, heterozygotes and homozygotes exhibited reduced axonal transport phenotypes. In addition, we developed *in vitro* assays to analyze the motility of single heterodimers composed of wild-type KIF1A and disease-associated KIF1A. Disease-associated KIF1A significantly inhibited the motility of wild-type KIF1A when heterodimers were formed. These data indicate the molecular mechanism underlying the dominant nature of *de novo* KAND mutations.

Keywords: axonal transport, KAND, neuropathy, kinesin, UNC-104, KIF1A

Significance Statement

KIF1A is a molecular motor that transports synaptic vesicle precursors in axons. Recent studies have identified many *KIF1A* mutations in congenital neuropathy patients; however, the molecular mechanism of pathogenesis remains elusive. This study established a model for KIF1A-associated neuronal disorder (KAND) in *Caenorhabditis elegans* to analyze the molecular and cell biology of the disease *in vivo*. This study also established *in vitro* single-molecule assays to quantitatively analyze the effect of KAND mutations when mutant KIF1A forms heterodimers with wild-type KIF1A. Our findings provide a foundation for future genetic screening and for drug screening to search for KAND treatments.

Introduction

Neuronal function depends on specific intracellular transport called axonal transport (1-3). Neurons transmit information via synaptic vesicles that accumulate at synapses (4). The constituents of synaptic vesicles are synthesized and assembled in the cell body and transported down axons to synapses. The transported organelle is called a synaptic vesicle precursor (5). KIF1A is a kinesin superfamily protein that transports synaptic vesicle precursors in axons (5, 6). KIF1A has a motor domain and a cargo-binding tail domain (5). The motor domain, which is conserved among Kinesin superfamily members, has microtubule-dependent ATPase activity that drives movement on microtubules (7, 8). The tail domain of KIF1A is composed of a protein-binding stalk domain and a lipid binding Pleckstrin-homology (PH) domain (6, 9-11).

Caenorhabditis elegans (*C. elegans*) is a good model animal to study axonal transport (12-19). UNC-104 is a *C. elegans* orthologue of KIF1A (20, 21). Electron and light microscopy analyses have shown that synapses as well as synaptic vesicles are mislocalized in *unc-104* mutants (20). The mechanism of axonal transport is well conserved between *C. elegans* and mammals and the expression of a human *Kif1a* cDNA can rescue the phenotype of *unc-104* mutant worms (22).

Mutations in the motor domain of *KIF1A* can cause congenital neuropathies (23, 24). More than 60 mutations have been found in the motor domain of *KIF1A* in neuropathy patients. Some cases are familial, but most are sporadic. For example, KIF1A(R11Q) was found in autism spectrum disorder and attention-deficit hyperactivity disorder (25), and KIF1A(R254Q) was found in Japanese spastic paraplegia patients (26). KIF1A(R254) is a hot spot for a broad range of neuropathies, such as KIF1A(R254W), have been described in non-Japanese patients (24). These neuropathies caused by KIF1A mutations is called KIF1A-associated neuronal disorder (KAND). Both dominant and recessive mutations are associated with KAND. KAND is caused by both gain of function and loss of function mechanisms. We have shown that familial mutations, KIF1A(V8M), KIF1A(A255V) and

KIF1A(R350G), over activate KIF1A and axonal transport. Recent *in vitro* studies have shown that *de novo* KAND mutations are loss of function. KIF1A(P305L) reduces the microtubule association rate of the motor (27). KIF1A(R169T) disrupts the microtubule-dependent ATPase activity of the motor domain (28). KIF1A(R254W) reduces the velocity and run length of the motor protein (24) .

While these loss of function mutations have been intensively studied using *in vitro* assays, reliable models to study the neuronal cell biology of KAND mutations *in vivo* are awaited. Moreover, previous *in vitro* studies have mostly analyzed homodimers composed of disease-associated KIF1A (24, 27) because it was difficult to purify heterodimers composed of wild-type and disease-associated KIF1A (29). Activated KIF1A forms a homodimer to move on microtubules (30); therefore, wild-type KIF1A is very likely to dimerize with disease-associated KIF1A in patient neurons. However, it is not known whether *de novo* KAND mutations inhibit the function of wild-type KIF1A in a dominant negative fashion.

Here, we established *C. elegans* models of *de novo* KAND mutations. Heterozygous worms, as well as homozygous worms, show synaptic deficiencies that are caused by axonal transport defects. We also established an *in vitro* single molecule analysis system to measure the motility parameters of a single heterodimer composed of wild-type and disease-associated KIF1A. Heterodimers composed of wild-type KIF1A and disease-associated KIF1A showed reduced motility *in vitro*.

Results

C. elegans models of *de novo* KAND

To study molecular and cellular deficiencies caused by *de novo* disease-associated KIF1A mutations, we established *C. elegans* models for KAND using CRISPR/cas9 (31). *C.elegnas unc-104* gene is an orthologue of human *Kif1a*. We introduced following mutations in *unc-104* gene: *unc-104(R9Q)*,

unc-104(R251Q) and *unc-104(P298L)* (Figure 1A and B). These *unc-104* residues are conserved in human KIF1A and these mutations correspond to KIF1A(R11Q), KIF1A(R254Q) and KIF1A(P305L) mutations, respectively. All of them are causes of *de novo* and autosomal dominant KAND (25-27). Introduction of mutations was confirmed by Sanger sequencing. Then, we observed the macroscopic phenotypes of disease model worms. The body size of homozygous worms was smaller than that of wild-type worms [1.09 ± 0.09 mm, 0.66 ± 0.06 mm, 0.64 ± 0.07 mm, 0.74 ± 0.06 mm, respectively for *wild type*, *unc-104(R9Q)*, *unc-104(R241Q)*, and *unc-104(P298L)*] (Figure 1C). Moreover, homozygous worms showed uncoordinated (unc) phenotypes and did not move well on the culture plate (Figure 1C). To quantitively analyze the movement of worms, the number of body bends in a water drop was counted during one minute (Figure 1D). We found homozygous worms did not move well in the water. These results collectively show that all three mutants phenocopy a well-established loss-of-function allele of *unc-104*, such as unc-*104(e1265)* (20), indicating that KIF1A(R11Q), KIF1A(R254Q) and KIF1A(P305L) mutations are loss of function.

Synaptic vesicles are mislocalized in homozygotes

UNC-104 is an orthologue of human KIF1A and is a molecular motor that determines the localization of synaptic vesicles in *C. elegans*; therefore, we visualized synaptic vesicles in KAND model worms. The DA9 neuron in *C. elegans* is highly polarized and forms *en passant* synapses along the dorsal side of the axon (32) (Figure 2A). The characteristic morphology of DA9 is suitable for analyzing axonal transport and synaptic localization (33). We expressed a synaptic vesicle marker GFP::RAB-3 in the DA9 neuron using the *itr-1* promoter to visualize DA9 synapses (Figure 2B). In KAND models, GFP::RAB-3 signals were reduced in the axon and misaccumulated in the dendrite (Figure 2C–F). Only a trace amount of GFP::RAB-3 signal was observed in the DA9 axon in KAND models.

We then observed axonal transport of synaptic vesicle precursors in the proximal region of the DA9 axon (33) (Figure 2A, magenta circle). We used GFP::RAB-3 as a representative marker for axonal transport of synaptic vesicle precursors because previous studies have shown that GFP::RAB-3 co-migrates with other synaptic vesicle and pre-synaptic proteins in the axon and is, therefore, a good marker to visualize axonal transport (6, 19, 33). In the wild-type worms, both anterograde and retrograde transport were observed in the axon (Figure 2G and H). In contrast, the frequency of both anterograde and retrograde events was significantly reduced in all three mutant strains (Figure 2G and H). In more than 70% of mutant worms, no vesicular movement was detected in the 30 sec time window. These data indicate that axonal transport of synaptic vesicles is strongly affected in *unc-104(R9Q)*, *unc-104(R251Q)* and *unc-104(P298L)* strains.

KAND mutations disrupt the motility of motor proteins *in vitro*

To study the effect of KAND mutations *in vitro*, we observed the motility of purified human KIF1A protein using total internal reflection fluorescence (TIRF) microscopy (34, 35). To directly study motility parameters, regulatory domains and cargo binding domains were removed (Figure 3A). The neck coiled-coil domain of mammalian KIF1A does not form stable dimers (36); therefore, we stabilized human KIF1A dimers using a leucine zipper domain as described previously (24, 27). A red fluorescent protein, mScarlet-I, was added to the C-terminus of the protein to observe movement (Figure 3A). Resultant KIF1A homodimers [KIF1A(1–393)::LZ::mSca] were purified by Strep tag and gel filtration (Figure 3B). This recombinant protein was then used to analyze the motility of single KIF1A dimers on microtubules (Figure 3C–J). The motility of KIF1A(1–393)::LZ::mSca dimers was observed at 10 pM (Figure 3C). KIF1A(1–393)(R11Q)::LZ::mSca did not move well on microtubules even at 100 pM (Figure 3D), while KIF1A(1–393)::LZ::mSca was saturated on microtubules under the same conditions (Figure

3G). KIF1A(1–393)(R254Q)::LZ::mSca moved on microtubules at 10 pM (Figure 3E). We observed frequent binding of KIF1A(1–393)(R254Q)::LZ::mSca with microtubules (Figure 3I) but the velocity was lower and the run length was shorter than for wild type (Figure 3H and J). The landing rate of KIF1A(1–393)(P305L)::LZ::mSca was significantly lower than wild type (Figure 3I), consistent with previous studies (24, 27). Although affected parameters were different depending on the mutated residues, these data are consistent with the reduced axonal transport phenotypes observed in KAND model worms.

Synaptic vesicles are mislocalized in heterozygous worms

KAND mutations, including KIF1A(R11Q), KIF1A(R254Q) and KIF1A(P305L) studied here, are *de novo* and cause neuropathies in an autosomal dominant manner. Moreover, KAND is a progressive disease. We therefore analyzed neuronal phenotypes of heterozygous worms in late adult stages (Figure 4A–F). DA9 synapses were analyzed in heterozygotes at 3 and 6 days after the final molt. The morphology of wild-type synapses was mostly maintained in 3 and 6-day-old adults (Figure 4A, C and E). More than 70% of wild-type worms did not show misaccumulation of GFP::RAB-3 in the proximal axon and dendrite at 3 and 6 days. However, 45 to 70% of *unc-104(R9Q)/+*, *unc-104(R251Q)/+* and *unc-104(P298L)/+* animals showed misaccumulation of GFP::RAB-3 in the proximal axon or dendrite (Figure 4B, D and E). To analyze the movement of heterozygous worms, the number of body bends in a water drop was counted for one minute at day 3, 6 and 9 (Figure 4F). The motility defects were not strong but there was a tendency for heterozygous worms to show reduced motility compared with wild-type worms.

Reduced Axonal transport in heterozygous worms

The DA9 axon and dendrite have plus-end out and minus-end out microtubules, respectively (37).

Thus, the mislocalization of synaptic vesicles in the proximal axon and dendrite indicate that anterograde transport is reduced in *unc-104(R9Q)/+*, *unc-104(R251Q)/+* and *unc-104(P298L)/+* worms. We therefore analyzed axonal transport of synaptic vesicle precursors visualized using GFP::RAB-3 in the DA9 axon as described above (Figure 2A). In *wild type*, *unc-104(R9Q)/+*, *unc-104(R251Q)/+* and *unc-104(P298L)/+* worms, both anterograde and retrograde movement of synaptic vesicle precursors was observed in the DA9 axon (Figure 5A–D). Vesicular movement in heterozygous worms was much better than that in homozygous worms (Figure 2). However, in mutant heterozygotes, the velocity of anterograde axonal transport was reduced. In contrast, retrograde transport, which depends on dynein motors, was not significantly changed in mutant heterozygotes. The frequency of both anterograde and retrograde axonal transport was reduced in mutant heterozygotes compared with that in wild type (Figure 5E–H).

Disease mutant/wild type heterodimers have reduced motor properties

The KIF1A motor forms a homodimer for efficient anterograde axonal transport (30). In heterozygotes, half of the motor complex in the neuron is predicted to be heterodimers composed of wild-type KIF1A and disease-associated KIF1A. But the behavior of heterodimers on microtubules remains largely unanalyzed. To analyze the motility of heterodimers at a single-molecule resolution, we purified heterodimers composed of wild-type KIF1A and disease-associated KIF1A. Wild-type KIF1A fused with leucine zipper and mScarlet-I [KIF1A(1–393)::LZ::mSca] and disease-associated KIF1A without fluorescent tag [KIF1A(1–393)::LZ] were co-expressed in bacteria (Figure 6A). The two constructs were respectively fused with a Strep tag and His tag for purification. Tandem affinity purification using His tag and Strep tag followed by gel filtration was performed to purify heterodimers. From a single peak, heterodimers composed of KIF1A(1–393)::LZ::mSca and KIF1A(1–393)::LZ were recovered (Figure 6B). The ratio between the two subunits was calculated

from band intensities and the molecular weights were about 1:1, indicating heterodimers.

As a positive control, we compared the motility of KIF1A(1–393)::LZ::mSca/KIF1A(1–393)::LZ heterodimers with KIF1A(1–393)::LZ::mSca homodimers (Figure 3C and 6C). Velocity, landing rate and run length of wild-type homodimers and heterodimers were statistically the same (velocity: 1.03 ± 0.24 µm/sec and 1.03 ± 0.26 µm /sec, run length: 7.99 ± 6.42 µm and 8.07 ± 6.30 µm, landing rate: 0.011 ± 0.003 $\mu m^{-1}s^{-1}$ and 0.010 ± 0.004 $\mu m^{-1}s^{-1}$ for homodimers and heterodimers respectively. Mean ± standard deviation). In contrast, heterodimers composed of wild-type KIF1A and disease-associated KIF1A showed reduced motility (Figure 6C–J). The velocity of KIF1A(1–393)::LZ::mSca/KIF1A(1–393)(R11Q)::LZ, KIF1A(1–393)::LZ::mSca/KIF1A(1–393)(R254Q)::LZ and KIF1A(1–393)::LZ::mSca/KIF1A(1–393)(P305L)::LZ heterodimers was lower than that of wild-type KIF1A (Figure 6H). The landing event of KIF1A(1–393)::LZ::mSca/KIF1A(1–393)(R11Q)::LZ and KIF1A(1–393)::LZ::mSca/KIF1A(1–393)(P305L)::LZ heterodimers on microtubules could not be observed at 10 pM (Figure 6I). At 100 pM, in which wild-type KIF1A homodimers were saturated on microtubules (Figure 6G), the motility of KIF1A(1–393)::LZ::mSca/KIF1A(1–393)(R11Q)::LZ and KIF1A(1–393)::LZ::mSca/KIF1A(1–393)(P305L)::LZ dimers was observed (Figure 6D, F and I) but the run lengths of these wild-type/mutant dimers were much shorter compared with that of wild-type dimers (Figure 6J). The landing rate of KIF1A(1–393)::LZ::mSca/KIF1A(1–393)(R254Q)::LZ heterodimers was higher than that of wild-type dimers (Figure 6I). However, run length of KIF1A(1–393)LZ-mSca/KIF1A(1–393)(R254Q)LZ heterodimers was shorter than that of wild-type dimers (Figure 6J). These results show that KAND mutations strongly affect the landing rate and motility parameters in heterodimers with wild-type KIF1A.

Finally, to show that a KAND mutation dominant negatively inhibits axonal transport *in vivo*, an *unc-104(R9Q)* cDNA corresponding to the KIF1A(R11Q) mutant, was overexpressed in the DA9 neuron (Figure 7A–C). In 70% of UNC-104(R9Q)-overexpressed animals, synaptic vesicles misaccumulated in the proximal region of the DA9 axon (Figure 7B and C). This phenotype is similar to a weak loss-of-function allele of *unc-104* (38), indicating that KAND mutations inhibit axonal transport by counteracting wild-type motor activity.

Discussion

Axonal transport motors form homodimers that move processively on microtubules (39). When a mutation in a motor protein gene is dominant, and if the mutation does not affect the stability or expression of the protein, half of the motor dimers in the cell are predicted to be heterodimers composed of wild-type motor and disease-associated motor. Many disease-associated mutations in motor proteins are caused by autosomal dominant mutations; however, little attention has been paid to the properties of heterodimers in motor-associated diseases (23, 24). We show here that disease-associated KIF1A perturbs the function of wild-type KIF1A by forming dimers. Interestingly, properties of mutant homodimers reflect the behavior of wild-type/mutant heterodimers (Figure 3 and 6). A previous study has analyzed the effect of heterodimerization in a semi-*in vitro* reconstitution in which motor proteins in COS-7 cell lysates, but not purified motor proteins, are observed (29). Some important phenomena, such as landing motor proteins on microtubules, cannot be quantitatively analyzed in the semi-*in vitro* reconstitution system because it is difficult to precisely control the concentration of motors. In our study, using purified heterodimers, we demonstrate that the landing rate of KIF1A(wt)/KIF1A(R11Q) and KIF1A(wt)/KIF1A(P305L) is significantly lower than that of wild-type KIF1A. As KIF1A(R11Q) and KIF1A(P305L) homodimers also have a much lower landing rate than wild-type KIF1A, these mutant subunits

inhibit the landing rate of wild-type subunits. KIF1A(R254Q) has a high landing rate and therefore inhibits wild-type KIF1A by a different mechanism, as described below. Mutations in other axonal transport motors, such as KIF5A and cytoplasmic dynein heavy chain 1 genes, are causes of autosomal dominant neuropathies (40-42). Similar phenomena to those observed here may underlie the pathogenesis of these neuropathies and it would be interesting to analyze heterodimers composed of wild-type and disease-associated motors in these cases. In the axon, multiple motors bind to and cooperatively transport a vesicle (43). Disease-associated KIF5A homodimers, which have lower motor activity than wild-type homodimers, inhibit the activity of wild-type KIF5A homodimers when mixed in the microtubule-gliding assay, which mimics cooperative transport (44). Considering this, both mutant KIF1A homodimers and wild-type/mutant KIF1A heterodimers, which both have lower motor activities (Figure 3 and 6), should dominant negatively perturb wild-type homodimers and axonal transport of cargo vesicles (Figure 7D). Consistent with this idea, overexpression of UNC-104(R9Q), mimicking KIF1A(R11Q), causes mislocalization of synaptic vesicles in wild-type neurons (Figure 7A–C). Reconstitution using a chassis composed of recombinant kinesins and DNA origami would help quantify how mutant homodimers and wild-type/mutant heterodimers inhibit axonal transport in KAND (45, 46).

Our worm models and single molecule analyses indicate that the velocity of axonal transport is affected by *de novo* autosomal dominant KAND mutations. The frequency of vesicle transport is reduced in disease worm models. Previous studies have suggested that the landing rate of KIF1A is a significant parameter in the pathogenesis of KAND (22, 27). KIF1A(V8M) and KIF1A(P305L) are gain of function and loss of function mutants with elevated and reduced landing rate, respectively. Our result of KIF1A(R11Q) having a significantly lower landing rate is consistent with these findings. Model worms expressing KIF1A(R11Q) showed reduced axonal transport. In contrast, KIF1A(R254Q) showed an elevated landing rate but its velocity and run length were

reduced. A previous study have shown that KIF1A dimers are faster than and have a much longer run length than another axonal transporter, KIF5 (47). Interestingly, the velocity of KIF1A(R254Q) shown here is comparable to that of KIF5 and the run length of KIF1A(R254Q) is still longer than that of KIF5. It is possible that the high velocity and/or the extremely long run length of KIF1A is fundamental to axonal transport of synaptic vesicle precursors, although the involvement of other parameters has not been completely excluded.

While homozygous disease model worms shows strong synaptic phenotypes, heterozygous model worms have clear but mild phenotypes (Figures 1 and 4). In the case of human, autosomal dominant KAND mutations cause severe neuropathies. These differences would arise from the fact that human has complicated neuronal networks and highly developed brain functions. Nevertheless, we think our worm model is useful. Currently, there is no good strategy for KAND treatment. *C. elegans* is a powerful tool to perform suppressor screening. We suggest that the worm models established here can be a foundation for genetic and drug screening to search for therapies to treat KAND.

Methods

Worm experiments

C. elegans strains were maintained as described previously (48). N2 wild-type worms and OP50 feeder bacteria were obtained from the *C. elegans* genetic center (CGC)(Minneapolis, MN, USA). Nematode growth medium agar plates were prepared as described (48). Transformation of *C. elegans* was performed by DNA injection as described (49). The swim test was performed as described previously (50).

Genome editing

Target sequences for cas9 and repair templates used to make *unc-104* mutants are described in ***supplementary table S1***. Target sequences were inserted into pRB1017 (a gift from Andrew Fire, Stanford University, addgene #59936). pDD162 (a gift from Bob Goldstein, UNC Chapel Hill, addgene #47549) was used to express Cas9. These vectors and oligonucleotides were injected into young adult worms as described with a slight modification (31). For *unc-104(R251Q)*, 50 ng of PDD162, 50 ng of unc-104(A252V)#4 and 0.6 μM of repair template were mixed and injected. Worms with a strong unc phenotype in the next generation were directly picked and genotyped by PCR. For *unc-104(R9Q)* and *unc-104(P298L)*, 50 ng of pDD162, 50 ng of sgRNA expression plasmid for *unc-104*, 50 ng of sgRNA expression plasmid for *ben-1*, and 0.6 μM of repair template for *unc-104* were mixed and injected. Injected worms were put on nematode growth medium plates with OP50 feeder bacteria supplemented with 10μg/ml benzoimidazole. The next generation was scored and benzoimidazole-resistant worms were picked and genotyped by PCR.

Strains

Strains used in this study are described in ***supplementary table S2***. Male worms carrying *wyIs85* and *wyIs251* were generated by a heat shock procedure. Heterozygotes were generated by crossing *unc-104* homozygotes with *wyIs85* or *wyIs251* males. Homozygotes show strong unc phenotypes, while heterozygotes do not. F1 worms showing non-unc phenotypes at the L4 stage were picked and transferred to new plates.

Statistical analyses and graph preparation

Statistical analyses were performed using Graph Pad Prism version 9. Statistical methods are described in the figure legends. Graphs were prepared using Graph Pad Prism version 9, exported in the TIFF format and aligned by Adobe Illustrator 2021.

337

338 ***Purification of homodimers***

339 Reagents were purchased from Nacarai tesque (Kyoto, Japan), unless described. Plasmids to express
340 recombinant KIF1A are described in ***supplementary table S3***. To purify
341 KIF1A(1–393)::LZ::mScarlet-I::Strep homodimers, BL21(DE3) was transformed and selected on
342 LB agar supplemented with kanamycin at 37°C overnight. Colonies were picked and cultured in 10
343 ml LB medium supplemented with kanamycin overnight. Next morning, 5 ml of the medium was
344 transferred to 500 ml 2.5× YT (20 g/L Tryptone, 12.5 g/L Yeast Extract, 6.5 g/L NaCl) supplemented
345 with 10 mM phosphate buffer (pH 7.4) and 50 μg/ml kanamycin in a 2 L flask and shaken at 37°C.
346 Two flasks were routinely prepared. When OD_{600} reached 0.6, flasks were cooled in ice-cold water
347 for 30 min. Then, 23.8 mg IPTG was added to each flask. Final concentration of IPTG was 0.2 mM.
348 Flasks were shaken at 18°C overnight.
349 Next day, bacteria expressing recombinant proteins were pelleted by centrifugation (3000 g, 10 min,
350 4°C), resuspended in PBS and centrifuged again (3000 g, 10 min, 4°C). Pellets were resuspended in
351 protein buffer (50 mM Hepes, pH 8.0, 150 mM KCH_3COO, 2 mM $MgSO_4$, 1 mM EGTA, 10%
352 glycerol) supplemented with Phenylmethylsulfonyl fluoride (PMSF). Bacteria were lysed using a
353 French Press G-M (Glen Mills, NJ, USA) as described by the manufacturer. Lysate was obtained by
354 centrifugation (75,000 g, 20 min, 4°C). Lysate was loaded on Streptactin-XT resin (IBA Lifesciences,
355 Göttingen, Germany) (bead volume: 2 ml). The resin was washed with 40 ml Strep wash buffer (50
356 mM Hepes, pH 8.0, 450 mM KCH_3COO, 2 mM $MgSO_4$, 1 mM EGTA, 10% glycerol). Protein was
357 eluted with 40 ml Strep elution buffer (50 mM Hepes, pH 8.0, 150 mM KCH_3COO, 2 mM $MgSO_4$, 1
358 mM EGTA, 10% glycerol, 300 mM biotin). Eluted solution was concentrated using an Amicon Ultra
359 15 (Merck) and then separated on an NGC chromatography system (Bio-Rad) equipped with a
360 Superdex 200 Increase 10/300 GL column (Cytiva). Peak fractions were collected and concentrated

using an Amicon Ultra 4 (Merck). Concentrated proteins were aliquoted and snap frozen in liquid nitrogen.

Purification of heterodimers

BL21(DE3) cells transformed with KIF1A(1–393)::LZ::mScarlet-I::Strep plasmid were cultured in LB supplemented with kanamycin at 37℃. Competent cells were prepared using a Mix&Go kit (Zymogen). The competent cells were further transformed with KIF1A(1–393)::LZ::His plasmid and selected on LB agar supplemented with ampicillin and kanamycin. Colonies were picked and cultured in 10 ml LB medium supplemented with ampicillin and kanamycin overnight. Next morning, 5 ml of the medium was transferred to 500 ml 2.5× YT supplemented with carbenicillin and kanamycin in a 2 L flask and shaken at 37°C. Two flasks were routinely prepared. The procedures for protein expression in bacteria and preparation of bacterial lysate were the same as for the purification of homodimers. Lysate was loaded on Streptactin-XT resin (bead volume: 2 ml). The resin was washed with 40 ml wash buffer. Protein was eluted with 40 ml protein buffer supplemented with 300 mM biotin. Eluted solution was then loaded on TALON resin (Takara Bio Inc., Kusatsu, Japan)(bead volume: 2 ml). The resin was washed with 40 ml His-tag wash buffer (50 mM Hepes, pH 8.0, 450 mM KCH_3COO, 2 mM $MgSO_4$, 10 mM imidazole, 10% glycerol) and eluted with His-tag elution buffer (50 mM Hepes, pH 8.0, 450 mM KCH_3COO, 2 mM $MgSO_4$, 10% glycerol, 500 mM imidazole). Eluted solution was concentrated using an Amicon Ultra 15 and then separated on an NGC chromatography system (Bio-Rad) equipped with a Superdex 200 Increase 10/300 GL column (Cytiva). Peak fractions were collected and concentrated using an Amicon Ultra 4. Concentrated proteins were aliquoted and snap frozen in liquid nitrogen.

TIRF single-molecule motility assays

TIRF assays were performed as described (22). Tubulin was purified from porcine brain as described (51). Tubulin was labeled with Biotin-PEG_2-NHS ester (Tokyo Chemical Industry, Tokyo, Japan) and AZDye647 NHS ester (Fluoroprobes, Scottsdale, AZ, USA) as described (52). To polymerize Taxol-stabilized microtubules labeled with biotin and AZDye647, 30 μM unlabeled tubulin, 1.5 μM biotin-labeled tubulin and 1.5 μM AZDye647-labeled tubulin were mixed in BRB80 buffer supplemented with 1 mM GTP and incubated for 15 min at 37°C. Then, an equal amount of BRB80 supplemented with 40 μM taxol was added and further incubated for more than 15 min. The solution was loaded on BRB80 supplemented with 300 mM sucrose and 20 μM taxol and ultracentrifuged at 100,000 g for 5 min at 30°C. The pellet was resuspended in BRB80 supplemented with 20 μM taxol. Glass chambers were prepared by acid washing as previously described (35). Polymerized microtubules were flowed into streptavidin adsorbed flow chambers and allowed to adhere for 5–10 min. Unbound microtubules were washed away using assay buffer [30 mM Hepes pH 7.4, 50 mM KCH_3COO, 2 mM $Mg(CH_3COO)_2$, 1 mM EGTA, 10% glycerol, 0.1 mg/ml biotin–BSA, 0.2 mg/ml kappa□casein, 0.5% Pluronic F127, 1 mM ATP, and an oxygen scavenging system composed of PCA/PCD/Trolox. Purified motor protein was diluted to indicated concentrations in the assay buffer. Then, the solution was flowed into the glass chamber. An ECLIPSE Ti2-E microscope equipped with a CFI Apochromat TIRF 100XC Oil objective lens, an Andor iXion life 897 camera and a Ti2-LAPP illumination system (Nikon, Tokyo, Japan) was used to observe single molecule motility. NIS-Elements AR software ver. 5.2 (Nikon) was used to control the system.

Data Availability

All study data are included in the article and/or supporting information.

Competing interest

409 The authors declare no competing interest.

410

411 **Author contribution**

412 S.N. designed research; Y.A., T.K and S.N. performed research; Y.A., T.K and S.N. analyzed data;

413 Y.A., T.K., K.H. and S.N. wrote the paper.

414

415 **Acknowledgements**

416 YA was supported by the Advanced Graduate Program for Future Medicine and Health Care, Tohoku

417 University. KH was supported by JST PRESTO (grant No. JPMJPR1877) and FRIS Creative

418 Interdisciplinary Research Program, Tohoku University. SN was supported by JSPS KAKENHI

419 (20H03247, 19H04738, 20K21378), the Naito foundation and the Uehara foundation. Some worm

420 strains and OP50 were obtained from the CGC. We thank Jeremy Allen, PhD, from Edanz

421 (https://jp.edanz.com/ac) for editing a draft of this manuscript.

422

423 **References**

424 1. S. Ochs, Fast transport of materials in mammalian nerve fibers. *Science* **176**, 252-260 (1972).

425 2. E. L. Holzbaur, S. S. Scherer, Microtubules, axonal transport, and neuropathy. *N Engl J Med* **365**,

426 2330-2332 (2011).

427 3. N. Hirokawa, Y. Noda, Y. Tanaka, S. Niwa, Kinesin superfamily motor proteins and intracellular

428 transport. *Nat Rev Mol Cell Biol* **10**, 682-696 (2009).

429 4. J. E. Heuser, T. S. Reese, Evidence for recycling of synaptic vesicle membrane during

430 transmitter release at the frog neuromuscular junction. *J Cell Biol* **57**, 315-344 (1973).

431 5. Y. Okada, H. Yamazaki, Y. Sekine-Aizawa, N. Hirokawa, The neuron-specific kinesin

432 superfamily protein KIF1A is a unique monomeric motor for anterograde axonal transport of

433 synaptic vesicle precursors. *Cell* **81**, 769-780 (1995).

434 6. S. Niwa, Y. Tanaka, N. Hirokawa, KIF1Bbeta- and KIF1A-mediated axonal transport of

435 presynaptic regulator Rab3 occurs in a GTP-dependent manner through DENN/MADD. *Nat Cell*

436 *Biol* **10**, 1269-1279 (2008).

437 7. M. Kikkawa *et al.*, Switch-based mechanism of kinesin motors. *Nature* **411**, 439-445 (2001).

8. R. Nitta, M. Kikkawa, Y. Okada, N. Hirokawa, KIF1A alternately uses two loops to bind microtubules. *Science* **305**, 678-683 (2004).
9. O. I. Wagner *et al.*, Synaptic scaffolding protein SYD-2 clusters and activates kinesin-3 UNC-104 in C. elegans. *Proc Natl Acad Sci U S A* **106**, 19605-19610 (2009).
10. D. R. Klopfenstein, R. D. Vale, The lipid binding pleckstrin homology domain in UNC-104 kinesin is necessary for synaptic vesicle transport in Caenorhabditis elegans. *Molecular Biology of the Cell* **15**, 3729-3739 (2004).
11. R. Stucchi *et al.*, Regulation of KIF1A-Driven Dense Core Vesicle Transport: Ca(2+)/CaM Controls DCV Binding and Liprin-alpha/TANC2 Recruits DCVs to Postsynaptic Sites. *Cell Rep* **24**, 685-700 (2018).
12. D. T. Byrd *et al.*, UNC-16, a JNK-signaling scaffold protein, regulates vesicle transport in C. elegans. *Neuron* **32**, 787-800 (2001).
13. Q. Zheng *et al.*, The vesicle protein SAM-4 regulates the processivity of synaptic vesicle transport. *PLoS Genet* **10**, e1004644 (2014).
14. S. Yogev, R. Cooper, R. Fetter, M. Horowitz, K. Shen, Microtubule Organization Determines Axonal Transport Dynamics. *Neuron* **92**, 449-460 (2016).
15. M. P. Klassen *et al.*, An Arf-like small G protein, ARL-8, promotes the axonal transport of presynaptic cargoes by suppressing vesicle aggregation. *Neuron* **66**, 710-723 (2010).
16. S. P. Koushika *et al.*, Mutations in Caenorhabditis elegans cytoplasmic dynein components reveal specificity of neuronal retrograde cargo. *J Neurosci* **24**, 3907-3916 (2004).
17. J. Kumar *et al.*, The Caenorhabditis elegans Kinesin-3 motor UNC-104/KIF1A is degraded upon loss of specific binding to cargo. *PLoS Genet* **6**, e1001200 (2010).
18. S. Niwa *et al.*, Autoinhibition of a Neuronal Kinesin UNC-104/KIF1A Regulates the Size and Density of Synapses. *Cell Rep* **16**, 2129-2141 (2016).
19. S. Niwa *et al.*, BORC Regulates the Axonal Transport of Synaptic Vesicle Precursors by Activating ARL-8. *Curr Biol* **27**, 2569-2578 e2564 (2017).
20. D. H. Hall, E. M. Hedgecock, Kinesin-related gene unc-104 is required for axonal transport of synaptic vesicles in C. elegans. *Cell* **65**, 837-847 (1991).
21. A. J. Otsuka *et al.*, The C. elegans unc-104 gene encodes a putative kinesin heavy chain-like protein. *Neuron* **6**, 113-122 (1991).
22. K. Chiba *et al.*, Disease-associated mutations hyperactivate KIF1A motility and anterograde axonal transport of synaptic vesicle precursors. *Proc Natl Acad Sci U S A* **116**, 18429-18434 (2019).
23. S. Esmaeeli Nieh *et al.*, De novo mutations in KIF1A cause progressive encephalopathy and brain atrophy. *Ann Clin Transl Neurol* **2**, 623-635 (2015).
24. L. Boyle *et al.*, Genotype and defects in microtubule-based motility correlate with clinical

severity in KIF1A-associated neurological disorder. *HGG Adv* **2** (2021).

25. T. Nemani *et al.*, KIF1A-related disorders in children: A wide spectrum of central and peripheral nervous system involvement. *J Peripher Nerv Syst* **25**, 117-124 (2020).

26. C. Ohba *et al.*, De novo KIF1A mutations cause intellectual deficit, cerebellar atrophy, lower limb spasticity and visual disturbance. *J Hum Genet* **60**, 739-742 (2015).

27. A. J. Lam *et al.*, A highly conserved 310 helix within the kinesin motor domain is critical for kinesin function and human health. *Sci Adv* **7** (2021).

28. C. Aguilera *et al.*, The Novel KIF1A Missense Variant (R169T) Strongly Reduces Microtubule Stimulated ATPase Activity and Is Associated With NESCAV Syndrome. *Front Neurosci* **15**, 618098 (2021).

29. B. G. Budaitis *et al.*, Pathogenic mutations in the kinesin-3 motor KIF1A diminish force generation and movement through allosteric mechanisms. *J Cell Biol* **220** (2021).

30. M. Tomishige, D. R. Klopfenstein, R. D. Vale, Conversion of Unc104/KIF1A kinesin into a processive motor after dimerization. *Science* **297**, 2263-2267 (2002).

31. J. A. Arribere *et al.*, Efficient marker-free recovery of custom genetic modifications with CRISPR/Cas9 in Caenorhabditis elegans. *Genetics* **198**, 837-846 (2014).

32. M. P. Klassen, K. Shen, Wnt signaling positions neuromuscular connectivity by inhibiting synapse formation in C. elegans. *Cell* **130**, 704-716 (2007).

33. C. I. Maeder, A. San-Miguel, E. Y. Wu, H. Lu, K. Shen, In vivo neuron-wide analysis of synaptic vesicle precursor trafficking. *Traffic* **15**, 273-291 (2014).

34. R. D. Vale *et al.*, Direct observation of single kinesin molecules moving along microtubules. *Nature* **380**, 451-453 (1996).

35. R. J. McKenney, W. Huynh, M. E. Tanenbaum, G. Bhabha, R. D. Vale, Activation of cytoplasmic dynein motility by dynactin-cargo adapter complexes. *Science* **345**, 337-341 (2014).

36. Y. Okada, N. Hirokawa, A processive single-headed motor: kinesin superfamily protein KIF1A. *Science* **283**, 1152-1157 (1999).

37. J. Yan *et al.*, Kinesin-1 regulates dendrite microtubule polarity in Caenorhabditis elegans. *Elife* **2**, e00133 (2013).

38. L. B. Li *et al.*, The Neuronal Kinesin UNC-104/KIF1A Is a Key Regulator of Synaptic Aging and Insulin Signaling-Regulated Memory. *Curr Biol* **26**, 605-615 (2016).

39. R. D. Vale, The molecular motor toolbox for intracellular transport. *Cell* **112**, 467-480 (2003).

40. M. G. Marzo *et al.*, Molecular basis for dyneinopathies reveals insight into dynein regulation and dysfunction. *Elife* **8** (2019).

41. E. Reid *et al.*, A kinesin heavy chain (KIF5A) mutation in hereditary spastic paraplegia (SPG10). *Am J Hum Genet* **71**, 1189-1194 (2002).

42. H. T. Hoang, M. A. Schlager, A. P. Carter, S. L. Bullock, DYNC1H1 mutations associated with

neurological diseases compromise processivity of dynein-dynactin-cargo adaptor complexes. *Proc Natl Acad Sci U S A* **114**, E1597-E1606 (2017).

43. K. Hayashi, S. Hasegawa, T. Sagawa, S. Tasaki, S. Niwa, Non-invasive force measurement reveals the number of active kinesins on a synaptic vesicle precursor in axonal transport regulated by ARL-8. *Phys Chem Chem Phys* **20**, 3403-3410 (2018).

44. B. Ebbing *et al.*, Effect of spastic paraplegia mutations in KIF5A kinesin on transport activity. *Hum Mol Genet* **17**, 1245-1252 (2008).

45. K. Furuta *et al.*, Measuring collective transport by defined numbers of processive and nonprocessive kinesin motors. *Proc Natl Acad Sci U S A* **110**, 501-506 (2013).

46. N. D. Derr *et al.*, Tug-of-war in motor protein ensembles revealed with a programmable DNA origami scaffold. *Science* **338**, 662-665 (2012).

47. V. Soppina *et al.*, Dimerization of mammalian kinesin-3 motors results in superprocessive motion. *Proc Natl Acad Sci U S A* **111**, 5562-5567 (2014).

48. S. Brenner, The genetics of Caenorhabditis elegans. *Genetics* **77**, 71-94 (1974).

49. C. C. Mello, J. M. Kramer, D. Stinchcomb, V. Ambros, Efficient gene transfer in C.elegans: extrachromosomal maintenance and integration of transforming sequences. *EMBO J* **10**, 3959-3970 (1991).

50. J. T. Pierce-Shimomura *et al.*, Genetic analysis of crawling and swimming locomotory patterns in C. elegans. *Proc Natl Acad Sci U S A* **105**, 20982-20987 (2008).

51. M. Castoldi, A. V. Popov, Purification of brain tubulin through two cycles of polymerization-depolymerization in a high-molarity buffer. *Protein Expr Purif* **32**, 83-88 (2003).

52. J. Al-Bassam, Reconstituting Dynamic Microtubule Polymerization Regulation by TOG Domain Proteins. *Method Enzymol* **540**, 131-148 (2014).

Figure legends

Figure 1 Establishment of disease model worms by genome editing

(A) Schematic drawing of the domain organization of KIF1A motor protein. NC, neck coiled-coil domain. CC1, Coiled-coil 1 domain. FHA, Forkhead-associated domain. CC2, Coiled-coil 2 domain. CC3, Coiled-coil 3 domain. PH, Pleckstrin-homology domain. The three KAND mutations and corresponding *C. elegans* UNC-104 mutations analyzed in this study are indicated.

(B) Sequence comparison between human KIF1A and *C. elegans* UNC-104.

(C) Macroscopic phenotypes of KAND model homozygotes. Mutant worms are smaller than wild-type worms and do not move well on the bacterial feeder. Bars, 1 mm.

(D) Swim test. The number of body bends in a water drop was counted for 1 min and plotted. Dots

represents data points. Green bars represent median values. Kruskal-Wallis test followed by Dunn's multiple comparison test. N = 20 worms for each genotype. **, adjusted P value < 0.01. ****, adjusted P value < 0.0001.

Figure 2 Synaptic vesicle localization in KAND model homozygous worms

(A) Schematic drawing show the morphology of the DA9 neuron. Green dots along the axon show synaptic vesicle distribution. The magenta circle shows the proximal axon.

(B–E) Representative images showing the distribution of synaptic vesicles in the DA9 neuron in *wild type* (B), *unc-104(R9Q)* (C), *unc-104(R251Q)* (D), and *unc-104(P298L)* (E). Synaptic vesicles are visualized by GFP::RAB-3. Arrowheads show mislocalization of synaptic vesicles in the dendrite and proximal axon. Bars, 50 μm.

(F) Dot plots showing the number of puncta in the axon (left panel) and dendrite (right panel) of DA9. Ordinary one-way ANOVA followed by Dunnett's multiple comparison test. Green bars show the mean ± standard deviation (S.D.). N = 60 worms for each genotype. ****, adjusted P value < 0.0001.

(G) Representative kymographs of *wild type* (upper panel) and *unc-104(R251Q)* (lower panel). The axonal transport of synaptic vesicle precursors was visualized by GFP::RAB-3. The proximal axon shown in panel (A) was observed. Vertical and horizontal bars show 10 seconds and 10 μm, respectively.

(H) Dot plots showing the frequency of anterograde axonal transport (left panel) and retrograde axonal transport (right panel). Green bars represent median values. Kruskal-Wallis test followed by Dunn's multiple comparison test. N = 14 *wild type*, 14 *unc-104(R9Q)*, 18 *unc-104(R251Q)* and 16 *unc-104(P298L)* axons. ****, adjusted P Value < 0.0001.

Figure 3 Single molecule behavior of disease-associated KIF1A mutants

(A) Schematic drawing of the domain organization of KIF1A motor protein and the recombinant protein analyzed in Figure 3.

(B) Purified KIF1A(1–393)::LZ::mScarlet and its mutants were separated by SDS-PAGE and detected by trichloroethanol staining. M represents a marker lane. Numbers on the left indicate molecular weight (kDa). Arrow indicates KIF1A(1–393)::LZ::mScarlet.

(C–G) Representative kymographs showing the motility of 10 pM KIF1A (wt) (C), 100 pM

575 KIF1A(R11Q) (D), 10 pM KIF1A(R254Q) (E), 100 pM KIF1A(P305L) and 100 pM KIF1A (wt)
576 (G). Vertical and horizontal bars represent 5 sec and 5 μm, respectively.
577 (H) Dot plots showing the velocity of KIF1A. Each dot indicates one datum. Green bars represent
578 median values. Kruskal-Wallis test followed by Dunn's multiple comparison test. n = 433 (wt), 325
579 (R254Q) and 498 (P305L). ****, adjusted P Value < 0.0001. Note that no processive movement was
580 detected for KIF1A(R11Q).
581 (I) Dot plots showing the landing rate of KIF1A. The number of KIF1A that bound to microtubules
582 was counted and adjusted by the time window and microtubule length. Each dot shows one datum.
583 Green bars represent median values. Kruskal-Wallis test followed by Dunn's multiple comparison
584 test. n = 30 (10 pM wt), 28 (100 pM R11Q), 29 (10 pM R254Q) and 30 (100 pM P305L) movies.
585 ****, adjusted P Value < 0.0001. Note that no landing event was detected in 10 pM KIF1A(R11Q)
586 and KIF1A(P305L) experiments.
587 (J) Dot plots showing the run length of KIF1A. Each dot shows one datum. Green bars represent
588 median values with interquartile ranges. Kruskal-Wallis test followed by Dunn's multiple
589 comparison test. n = 312 (wt), 241 (R254Q) and 243 (P305L) homodimers. ****, adjusted P Value <
590 0.0001.
591
592 **Figure 4 Synaptic vesicle localization of heterozygotes**
593 (A–D) Representative images showing synaptic vesicle distribution in 3 day-day-old *wild-type* adult
594 (A), 3 day-day-old *unc-104(R251Q)/+* adult (B), 6 day-day-old *wild-type* adult (C), and 6
595 day-day-old *unc-104(R251Q)/+* adult (D). Synaptic vesicles are visualized by GFP::RAB-3. Bars,
596 50 μm.
597 (E) The ratios of worms with dendritic mislocalization of synaptic vesicles to worms showing
598 wild-type localization of synaptic vesicles are shown. Chi-square test adjusted by Bonferroni
599 correction. *, adjusted P Value < 0.05. **, adjusted P Value < 0.01. ****, adjusted P Value < 0.0001.
600 (F) Dot plots showing swim test results at 3, 6 and 9 days-old. Each dot shows one datum. Green
601 bars represent median values. Kruskal-Wallis test followed by Dunn's multiple comparison test. N =
602 34 (wt), 38 (R9Q/+), 32 (R251Q/+) and 35 (P298L/+) (3-day-old adult worms); 36 (wt), 33 (R9Q/+),
603 36 (R251Q/+) and 35 (P298L/+) (6-day-old adult worms); 27 (wt), 30 (R9Q/+), 29 (R251Q/+) and
604 33 (P298L/+) (9-day-old adult worms). ns, adjusted P Value > 0.05 and statistically not significant. *,
605 adjusted P Value < 0.05. **, adjusted P Value < 0.01. ****, adjusted P Value < 0.0001.

Figure 5 Axonal transport in KAND model heterozygotes

(A–D) Representative kymographs showing axonal transport of synaptic vesicle precursors in *wild type* (A), *unc-104(R9Q)/+* (B), *unc-104(R251Q)/+* (C) and *unc-104(P305L)/+* (D). GFP::RAB-3 was used as a marker. Vertical and horizontal bars indicate 10 seconds and 10 μm, respectively.

(E and F) The velocity of axonal transport. The velocity of anterograde transport (E) and retrograde transport (F) are shown as dot plots. (E) Ordinary one-way ANOVA followed by Dunnett's multiple comparison test. Green bars show the mean ± S.D.. n = 94 (wild-type), 90 (R9Q/+), 66 (R251Q/+) and 117 (P298L/+) vesicles from at least five independent worms. ****, adjusted P Value < 0.0001. (F) Ordinary one-way ANOVA followed by Dunnett's multiple comparison test. Green bars show the mean ± S.D.. n = 63 (wild-type), 54 (R9Q/+), 38 (R251Q/+) and 53 (P298L/+) vesicles from at least five independent worms. ns, adjusted P Value > 0.05 and no significant statistical difference.

(G and H) Frequency of axonal transport. The frequency of anterograde transport (G) and retrograde transport (H) are shown as dot plots. (G) Kruskal-Wallis test followed by Dunn's multiple comparison test. Each dot represents data from each worm. Green bars represent median values. N = 14 (wt), 16 (R9Q/+), 18 (R251Q/+) and 19 (P298L/+) independent worms. ****, adjusted P Value < 0.0001. (H) Kruskal-Wallis test followed by Dunn's multiple comparison test. Each dot represents data from each worm. Green bars represent median values. N = 14 (wt), 16 (R9Q/+), 18 (R251Q/+) and 19 (P298L/+) independent worms. **, adjusted P Value < 0.01, ****, adjusted P Value < 0.0001.

Figure 6 The single molecule behavior of wild type/mutant KIF1A heterodimers

(A) Schematic drawing of the recombinant KIF1A heterodimer analyzed in Figure 6.

(B) Purified KIF1A(1–393)::LZ::mScarlet/KIF1A(1–393)::LZ heterodimers were separated by SDS-PAGE and detected by Coomassie brilliant blue staining. M represents marker. Numbers on the left indicate the molecular weight (kDa). Magenta and black arrows indicate KIF1A(1–393)::LZ::mScarlet and KIF1A(1–393)::LZ, respectively.

(C–G) Representative kymographs showing the motility of 10 pM KIF1A (wt) (C), 100 pM KIF1A(R11Q) (D), 10 pM KIF1A(R254Q) (E), 100 pM KIF1A(P305L) and 100 pM KIF1A (wt) (G). Vertical and horizontal bars represent 5 sec and 5 μm, respectively.

(H) Dot plots showing the velocity of KIF1A. Each dot shows one datum. Green bars represent median values. Kruskal-Wallis test followed by Dunn's multiple comparison test. n = 308 (wt/wt),

315 (wt/R11Q), 294 (wt/R254Q) and 414 (wt/P305L) heterodimers. ****, adjusted P Value < 0.0001.

(I) Dot plots showing the landing rate of KIF1A. The number of KIF1A molecules that bind to microtubules was counted and adjusted by the time window and microtubule length. Each dot shows one datum. Green bars represent median values. Kruskal-Wallis test followed by Dunn's multiple comparison test. n = 29 (10 pM wt/wt), 29 (100 pM wt/R11Q), 28 (10 pM wt/R254Q) and 38 (100 pM wt/P305L) independent observations. **, adjusted P Value < 0.01, ***, adjusted P Value < 0.001, ****, adjusted P Value < 0.0001.

(J) Dot plots showing the run length of KIF1A. Each dot shows one datum. Green bars represent median values and interquartile ranges. Kruskal-Wallis test followed by Dunn's multiple comparison test. n = 215 (wt/wt), 241 (wt/R11Q), 195 (wt/R254Q) and 266 (wt/P305L) heterodimers. ****, adjusted P Value < 0.0001.

Figure 7 KAND mutations inhibit axonal transport in a dominant negative fashion

(A–C) UNC-104(R9Q) was overexpressed in the *wild-type* background and the localization of synaptic vesicles was observed. (A and B) Representative images showing the localization of synaptic vesicles in *wild-type* (A) and UNC-104(R9Q)-overexpressing worms (B). Arrow heads show synaptic-vesicle accumulated puncta that are mislocalized in the proximal region of the axon. Bars, 50 μm. (C) Bar graphs showing the ratio of affected animals. Chi-square test. N = 51 (*wt*) and 49 [unc-104(R9Q)-overexpressing worm]. ****, p < 0.0001.

(D) Schematic drawing showing how vesicular transport is suppressed in KAND patient axons. Not only mutant homodimers but also wild-type/mutant heterodimers inhibit axonal transport of synaptic vesicle precursors.

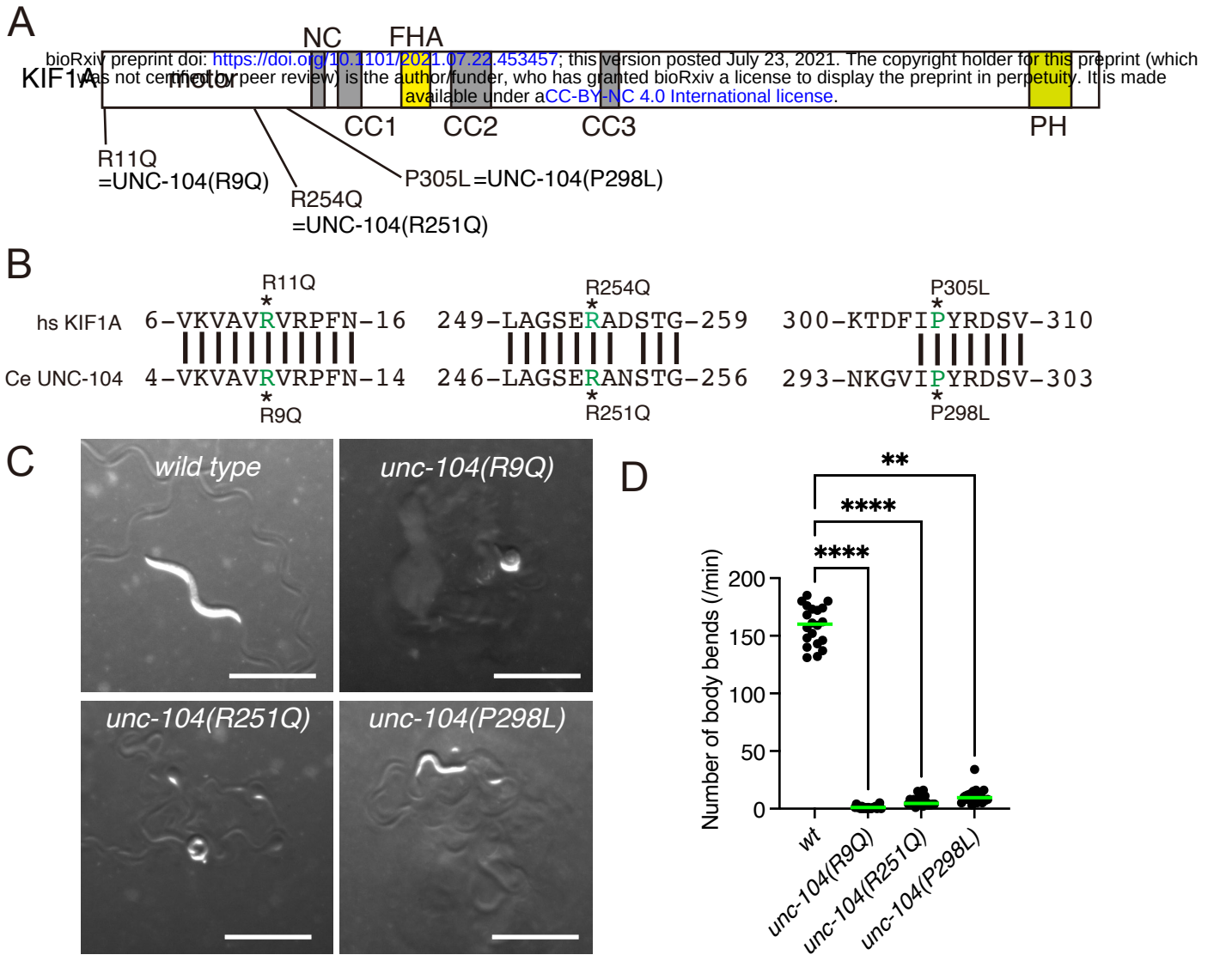

Figure 1

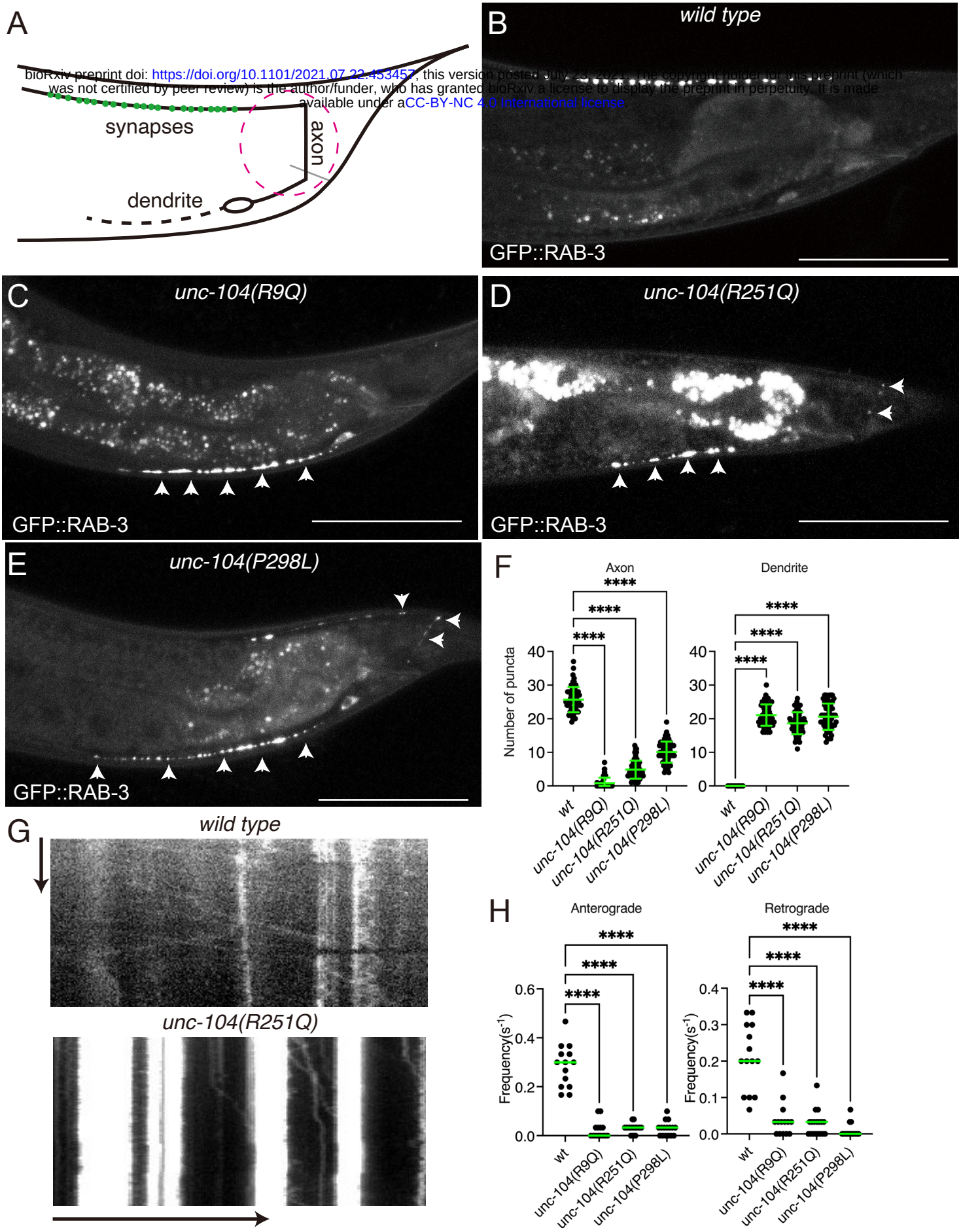

Figure 2

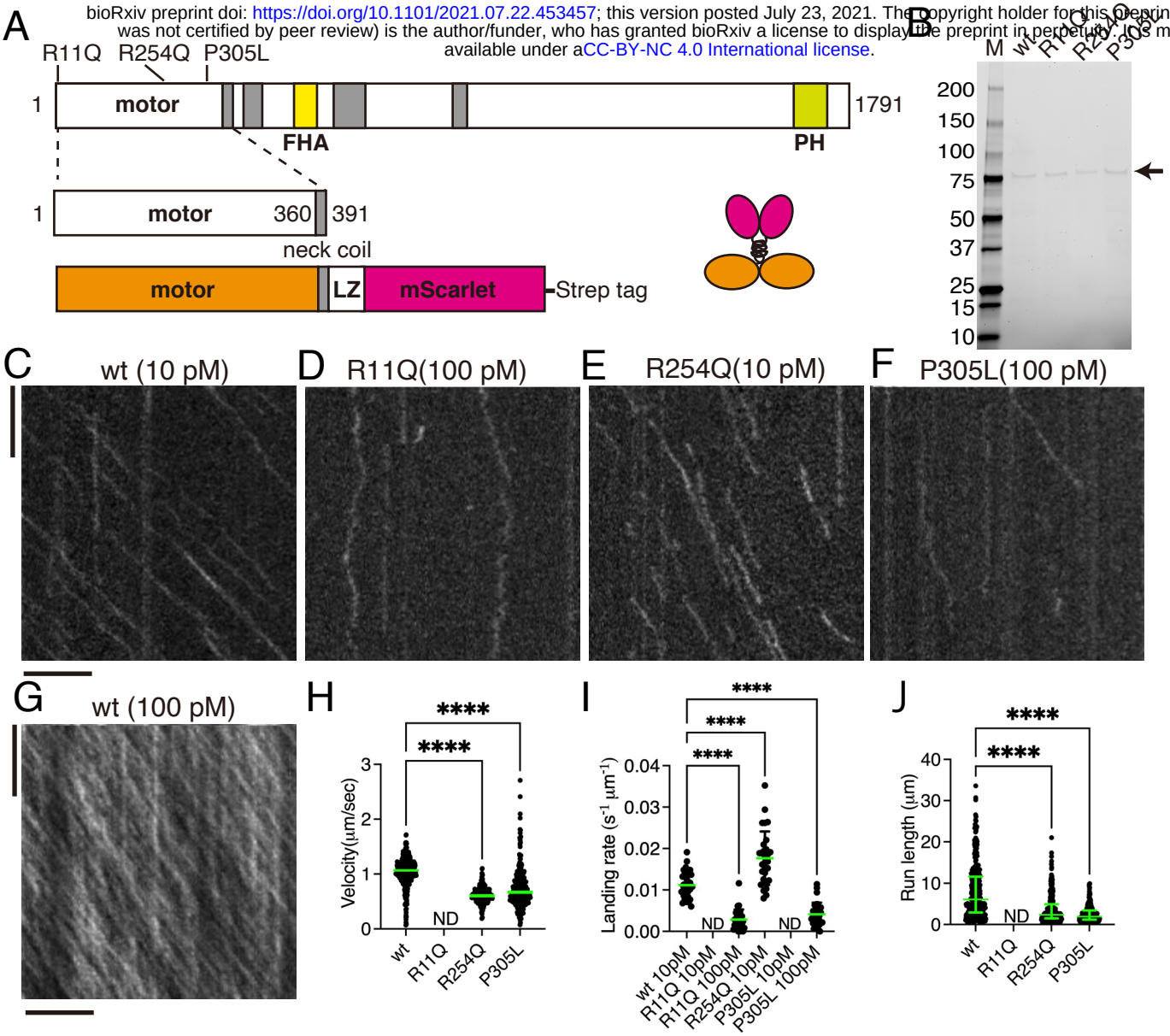

Figure 3

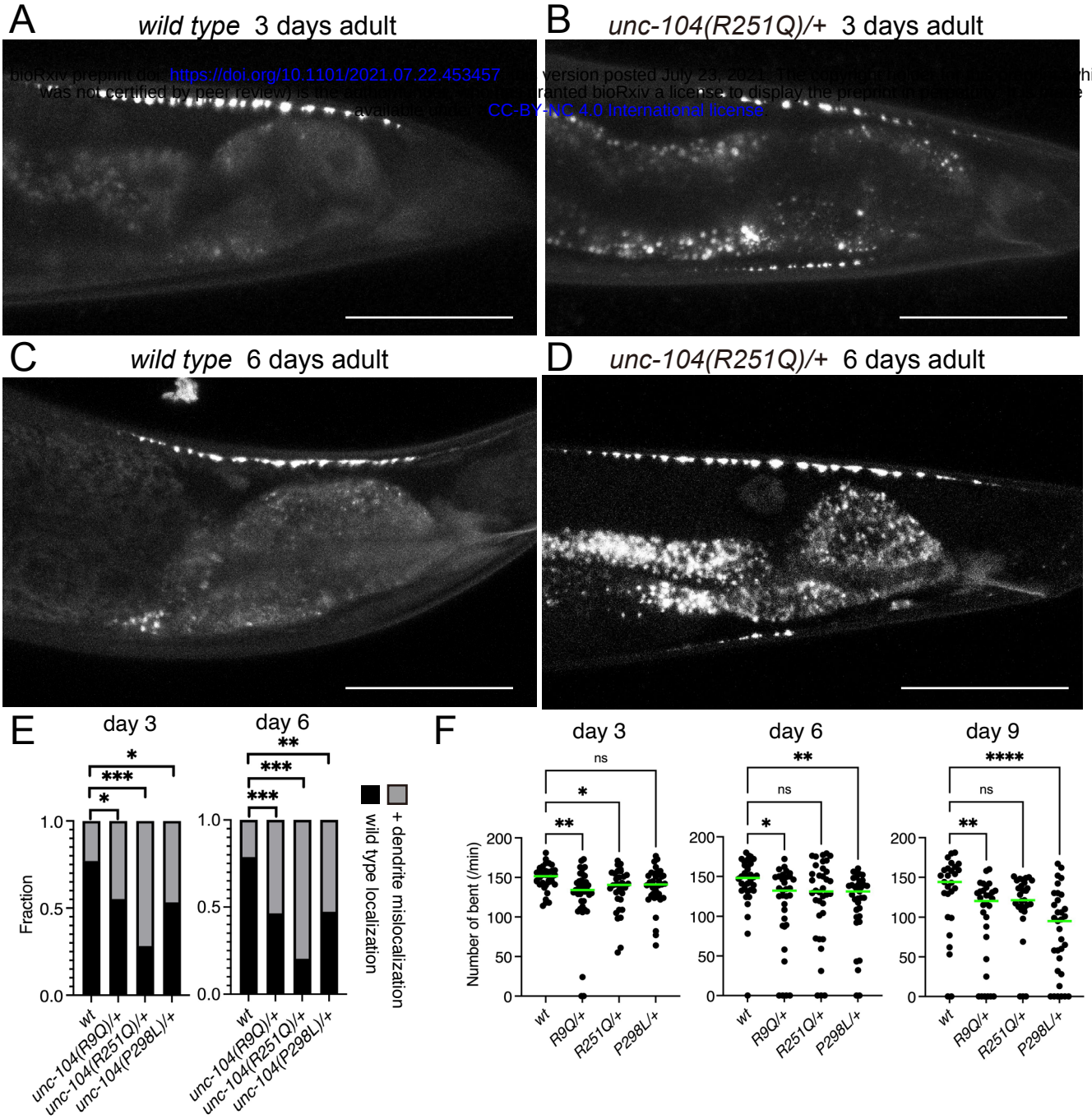

Figure 4

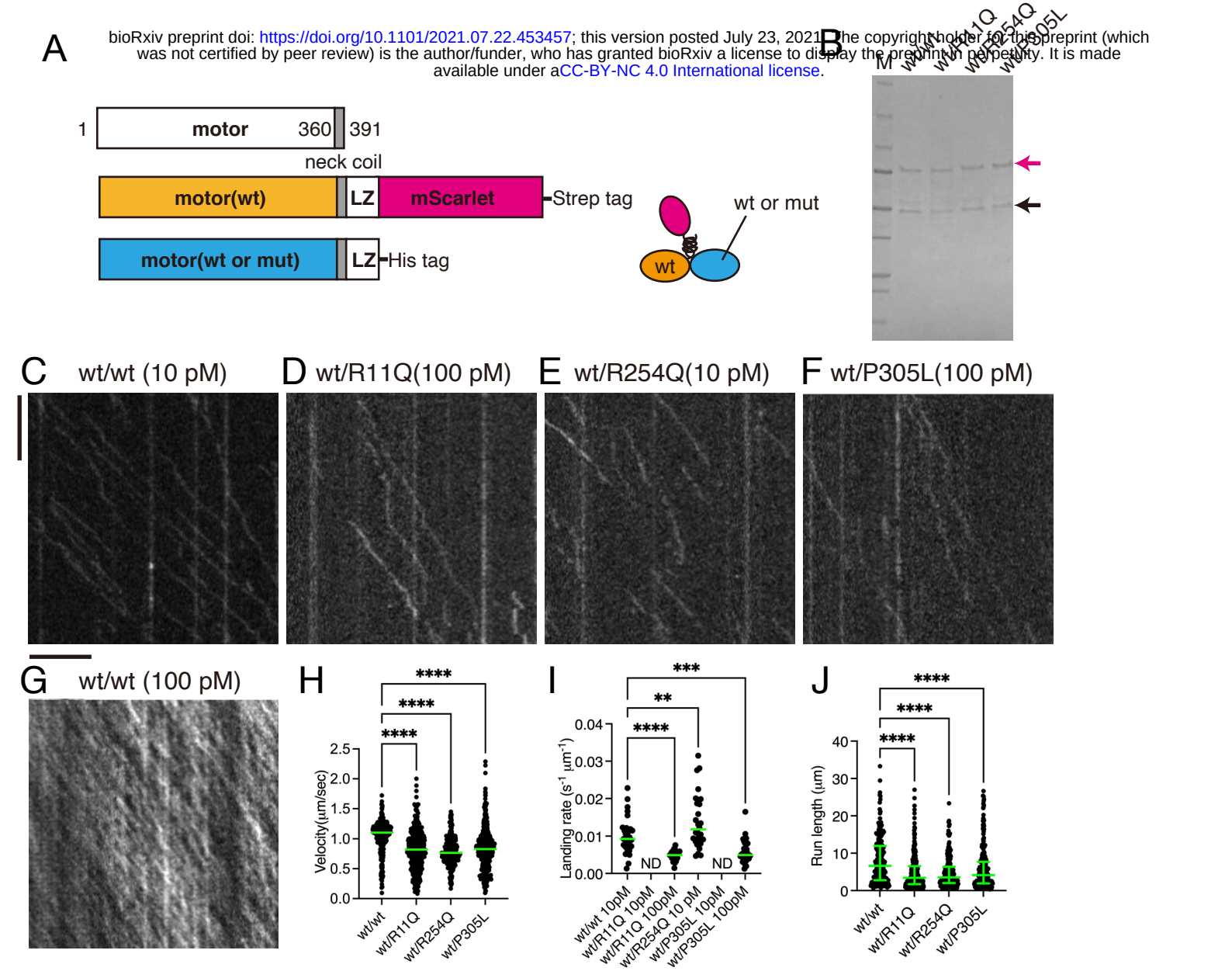

Figure 5

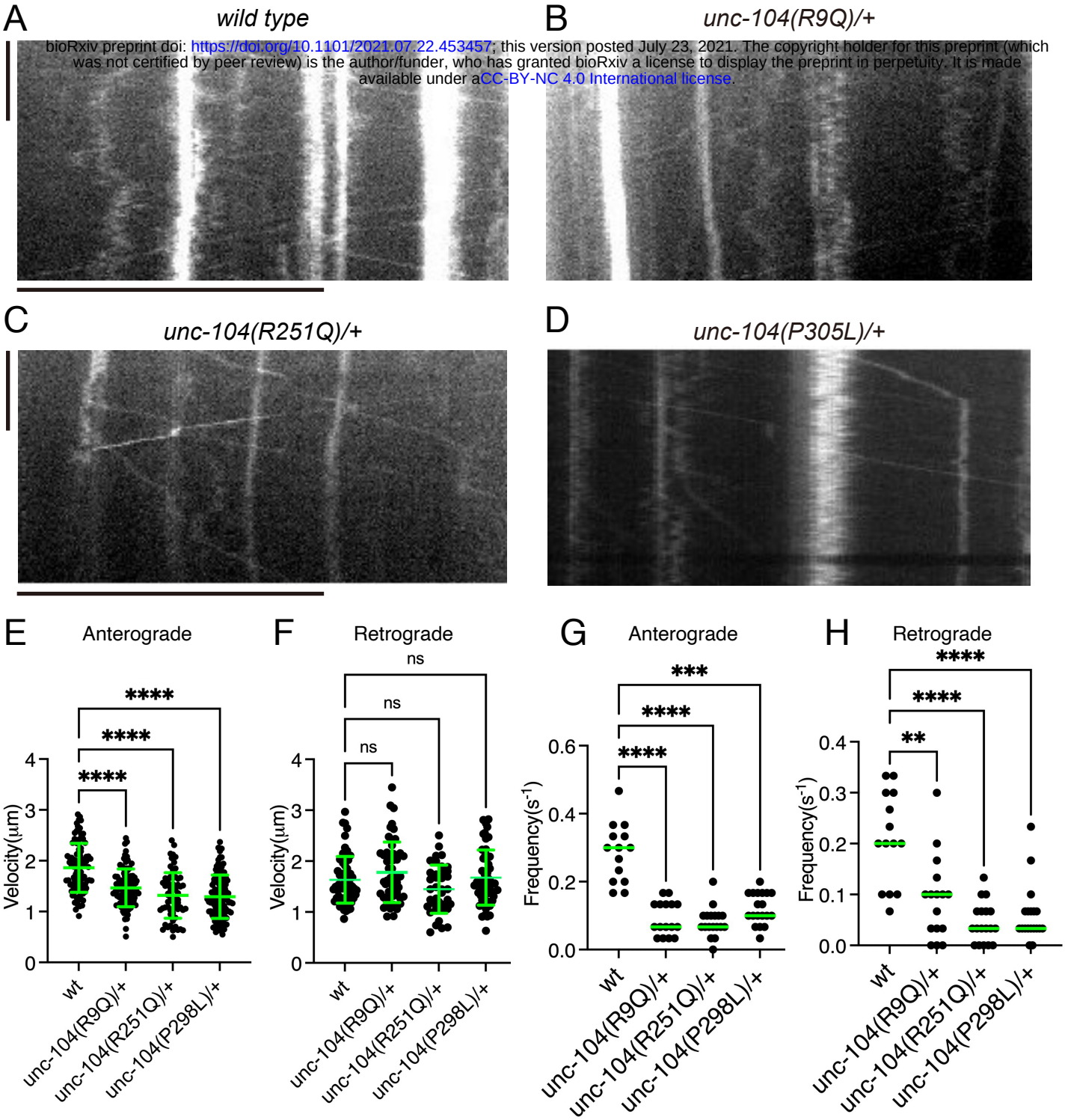

Figure 6

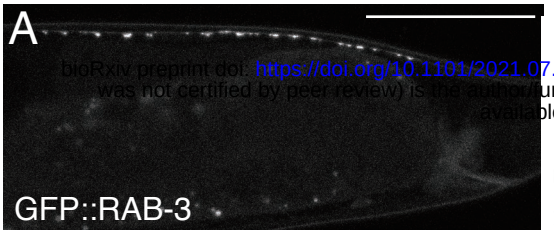

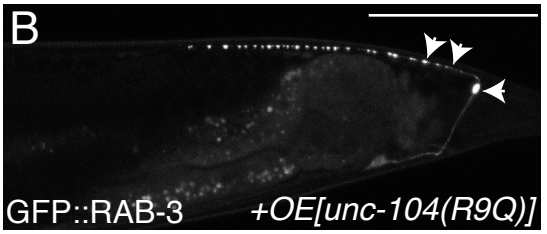

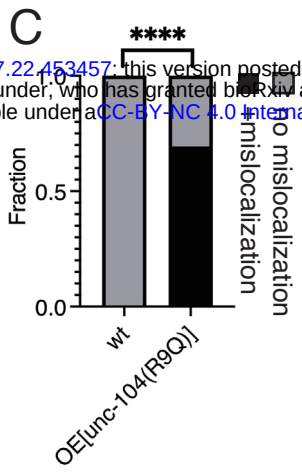

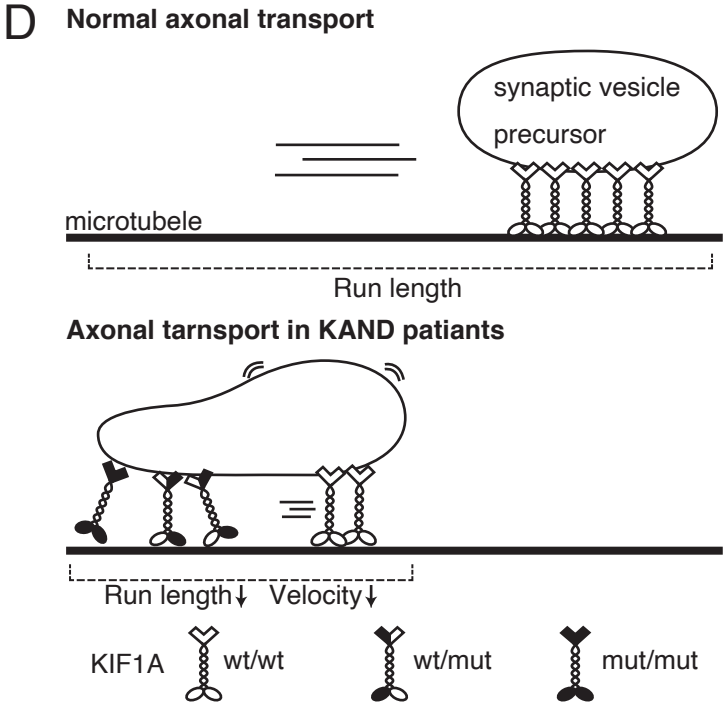

Figure 7